Synchronous Commutation Control of Doubly Salient Motor Drive With Adaptive Angle Optimization

Zhangming Bian, Zhuoran Zhang, *Senior Member, IEEE*, and Li Yu, *Member, IEEE*

***Abstract*—Due to the strong nonlinearity of the commutation process of doubly salient motors fed by square-wave currents, it is difficult to establish accurate models and design an appropriate commutation control strategy to achieve satisfactory commutation performance. The synchronous commutation control method is proposed to improve commutation control. By introducing an additional angle loop to synchronize the zero crossings of the phase current and the alignment of the core poles, the commutation angle can be adaptively optimized without requiring the accurate model. Also presented is a vector control scheme during the commutation process to shape the trajectory of the current vector into a regular hexagon. Based on the linearized model of the commutation process, the digital control law to synchronize the zero crossings is designed with robustness considered. Finally, simulations and experiments were conducted. The results show less commutation torque loss with the method. Ultimately, the method provides a high torque-to-current ratio and low-torque ripple at a wide range of speeds.**

***Index Terms*—Doubly salient motor, synchronous commutation control (SCC), torque-to-current ratio, torque ripple, vector control.**

I. Introduction

A DOUBLY salient machine (DSM) is a reluctance machine that is marked by a doubly salient core structure and concentrated stator excitation [1], [2]. The absence of windings or permanent magnets in the rotor ensures robust operation at high speeds and also offers manufacturing convenience and low cost. Thus, this machine has raised research interest for use in aviation and electric vehicles.

Ideally, this machine is driven by a square-wave current [1], [3]. However, when the speed is high, the inverter cannot provide high enough di/dt, and the current commutation process should be considered. Then, there is a phase delay of current and a decrease in the inner power factor of the motor. As a result, a commutation torque ripple is produced, and the torque-to-current ratio is reduced.

The commutation angles are advanced to compensate for the phase delay and weaken the resistance of back electromotive force (EMF) to current alternation [3]–[5]. The commutation process of a DSM is influenced by operating conditions, such as speed, field current, and load torque. The advanced angles should be optimized considering all variations. Angle optimization methods (AOMs) are categorized into model-based and search-based types. Model-based AOMs are carried out by building the mapping relationships between the operation parameters and the optimal advanced angle based on the model of the commutation process. One approach is analytical: restrictions and optimization goals are expressed by equations, and optimal solutions are obtained by solving conditional extremum problems. However, it is quite hard for the nonlinear DSM system to be expressed and solved analytically; therefore, simplified linear models are used [6], [7]. Another approach is numerical: the original data are collected by a numerical simulation or prototype test [3], [4], [7], and then, the optimization is carried out offline by numerical algorithms, including an artificial intelligence algorithm [8]. When implemented in microcontrollers, model-based AOMs need online calculation of functions or interpolation of lookup tables. However, in practice, the motor usually cannot work at the optimal point due to uncontrollable conditions, such as the differences in motor characteristics caused by machining errors, differences in parasitic inductances and resistances, temperature variations, and material aging. In order to make the advanced angle adaptive in practical applications, the optimal angles should be automatically searched for by trial and error online. Compared to model-based AOMs, search-based AOMs treat all unknowns as disturbances, and less model information is required. However, an adaptive system should be established and modeled that can effectively observe and optimize the performance index by regulating angles in real time. A certain amount of model information is still needed to design a loop controller so that the system with the additional loop has desirable stability, steady state, and dynamic performance. The model for a search-based AOM is simpler and easier to build than for a model-based AOM.

The performance deterioration during commutation originates from the phase delay of current. Therefore, a reasonable approach to implementing a search-based AOM is closed-loop phase delay compensation (CLPDC). So far, few studies have been conducted on the CLPDC of DSMs. We can draw inspiration from other synchronous machines. In sinusoidal synchronous motors, the phase angle is fed back as the direction

Manuscript received July 3, 2019; revised August 15, 2019; accepted October 15, 2019. Date of publication October 22, 2019; date of current version February 20, 2020. This work was supported in part by the National Natural Science Foundation for Excellent Young Scholar of China under Award 51622704, in part by the project by the State Key Program of the National Natural Science Foundation of China under Grant 51737006, and in part by the Postgraduate Innovation Base (Laboratory) Open Fund Project under Grant kfjj20180306. Recommended for publication by Associate Editor B. Singh. *(Corresponding author: Zhuoran Zhang.)*

The authors are with the College of Automation Engineering, Nanjing University of Aeronautics and Astronautics, Jiangsu 211106, China (e-mail: 951163479@qq.com; apsc-zzr@nuaa.edu.cn; yulipc@126.com).

Color versions of one or more of the figures in this article are available online at http://ieeexplore.ieee.org.

Digital Object Identifier 10.1109/TPEL.2019.2949095

of the current vector, and a CLPDC is naturally achieved by conventional vector control. In brushless dc motors (BLDCMs), CLPDC is based on the phase-locked loop technology [9], [10]. In switched reluctance motors (SRMs), turn-ON angles are adaptively advanced to compensate for the angle delay of the current rising process [11]–[13].

Apart from the commutation angles, the three-phase current should be well shaped during the commutation to reduce the commutation torque loss. However, the phase winding of a DSM is usually star connected and supplied by the full-bridge inverter, with no neutral point connected. Hence, the three-phase current usually cannot be controlled independently. Independent controls can be realized by connecting the neutral point to the bus split capacitors [3] or simply using three single-phase inverters, but these require, respectively, additional capacitor charge control and power switches. Due to the similarity in the current shape and converter topology, the commutation control of BLDCMs can be consulted. It has been reported that the vector control based on the coordinate transform theory can shape the current well and improve commutation of the BLDCM [14]. However, since a DSM has unbalanced nonlinear three-phase inductance and back EMF, the voltage vector should be carefully selected to shape the three-phase current and provide a large d*i*/d*t*, especially when the commutation duration is long.

This article proposes the synchronous commutation control (SCC) method, through which the phase delay is adaptively compensated, and the three-phase currents during the commutation are well shaped. The electrically excited DSM is studied in this article, but the method can be extended to the permanent magnet DSM. The presentation starts with the one-phase case in Section II, where the mathematical model of the commutation process is analyzed and the search-based optimization of advanced angle is discussed. Then, in Section III, the work is extended to the three-phase case, and the vector control strategy is presented. In Section IV, the closed-loop digital control law is designed based on the linearized model. The implementation and verification are shown in Sections V and VI, respectively. Conclusion is given in Section VII.

II. Single-Phase Analysis of the Commutation, Angle Control, and Synchronized Zero Crossing

A. Mathematical Model of the Commutation Process

Since the mutual inductance between the phase windings of a DSM is small, the current of each phase can be controlled independently. In this section, the commutation is analyzed without taking into consideration the mutual influence between phases.

Fig. 1 shows the simplified single-phase structure of the DSM. Ignoring the saturation, the flux linkage of the phase winding is expressed as

$$\psi_p\left(i_p, i_f, \theta\right) = L_p\left(\theta\right) i_p\left(\theta\right) + L_{pf}\left(\theta\right) i_f\left(\theta\right) \tag{1}$$

where ψ_p (p denotes a, b, or c in three-phase motors) is the flux linkage of the phase winding, θ is the electric angle of rotor position, i_p is the phase current, i_f is the field current, L_p is the self-inductance of the phase winding, and L_{pf} is the mutual

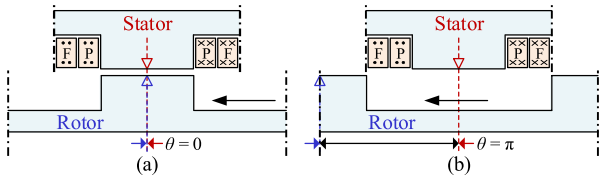

Fig. 1. Simplified single-phase structure of the DSM.

inductance between the phase winding and the field winding. L_{pf} can be linearized as

$$L_{pf}\left(\theta\right) = \begin{cases} k_{Lpf}\theta + L_{\text{pfmax}}, & -2\pi/3 < \theta < 0 \\ -k_{Lpf}\theta + L_{\text{pfmax}}, & 0 \le \theta < 2\pi/3 \\ L_{\text{pfmin}}, & \text{otherwise} \end{cases} \tag{2}$$

where

$$k_{Lpf} = \left(L_{\text{pfmax}} - L_{\text{pfmin}}\right) / \left(2\pi/3\right) \tag{3}$$

where L_{pfmax} and L_{pfmin} are the maximum L_{pf} and minimum L_{pf}, respectively. The relationship between L_p and L_{pf} is

$$L_p \approx L_{pf} N_p / N_f \tag{4}$$

where N_p is the turn number of the armature coil, and N_f is the turn number of the field coil. The phase torque is expressed as

$$T_p = \frac{1}{2} i_p^2 dL_p/d\theta_m + i_p i_f dL_{pf}/d\theta_m = T_{pr} + T_{pf} \tag{5}$$

where $\theta_m = N_r\theta$ is the mechanical angle of rotor position, and N_r is the pole number of the rotor. The first term T_{pr} is the reluctance torque, which is usually ignored in analysis [1]. The second term T_{pf} is the excitation torque.

The ideal L_{pf} is the triangular wave with flat bottom shown in Fig. 2(a). According to the value of $dL_{pf}/\mathrm{d}\theta$ under the different θ, the electric cycle is divided into three regions. When $\theta \in (\pi, -2\pi/3) \cup (2\pi/3, \pi)$, $dL_{pf}/\mathrm{d}\theta$ is 0, so no torque can be produced by the phase current. When $\theta \in (-2\pi/3, 0)$, $dL_{pf}/\mathrm{d}\theta$ is positive, so the positive current can produce positive excitation torque. When $\theta \in (0, -2\pi/3)$, $dL_{pf}/\mathrm{d}\theta$ is negative, so the negative current can produce positive excitation torque. The ideal square-wave current is shown in Fig. 2(a).

Ignoring the voltage drop across the resistance and assuming that the field current is constant, the voltage equation of the phase winding is

$$\begin{aligned} u_p = \frac{d\psi_p}{dt} &= \omega\left(L_p\frac{di_p}{d\theta} + i_p\frac{dL_p}{d\theta} + i_f\frac{dL_{pf}}{d\theta}\right) \\ &= e_{pt} + e_{pr} + e_{pf} \end{aligned} \tag{6}$$

where u_p is the voltage of the phase winding, ω is the angular velocity that is defined by $\mathrm{d}\theta/\mathrm{d}t$, e_{pr} and e_{pf} are the rotational EMFs, and e_{pt} is the transformer EMF.

Fig. 2(b) shows the waveforms with the commutation process, where the current has seven states that are divided by the seven commutation angles α_{on}, γ_{on}, α_{rvs}, γ_{rvs}, β_{rvs}, α_{off}, and γ_{off}. State 2 is the turn-ON commutation, states 4 and 5 are the turn-reverse commutation, and state 7 is the turn-OFF commutation.

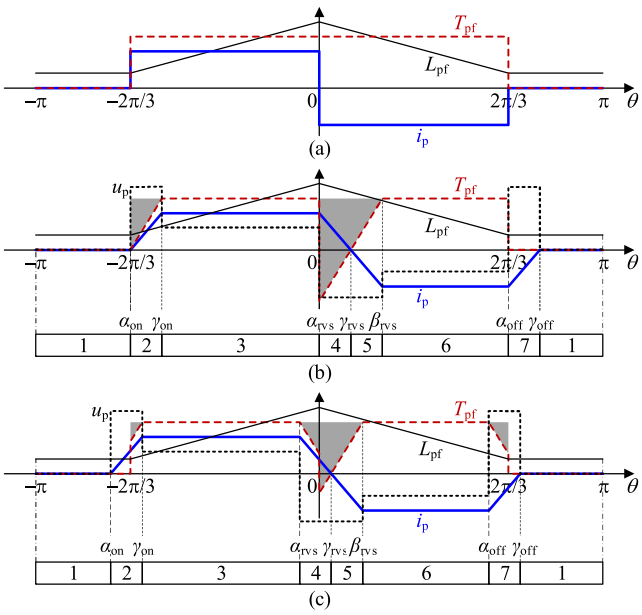

Fig. 2. Controlled current waves. (a) Advanced angle = 0, ideal square-wave current. (b) Advanced angle = 0, considering the current commutation. (c) Controlled advanced angle, considering the current commutation.

By rearranging (6), the current changing rate becomes

$$di_p/d\theta = (u_p - e_{pr} - e_{pf}) / (\omega L_p) . \tag{7}$$

During the commutation process, u_p should be controlled as the maximum or minimum for fast commutation. Usually, the voltage u_p is limited to the range $[-U, U]$ by the dc-bus voltage U. At high speed, the voltage difference between the dc-bus voltage and the rotational EMF is small, and the commutation reactance ωL_p is large. Therefore, it is hard for the current to alternate at high speed. The torque loss of the commutation, marked by the shaded area in Fig. 2(b), is large when the commutation time is long.

B. Advanced Angle Control

Fig. 2(c) illustrates the advanced angle control. The commutation angles are advanced to compensate for the phase delay and help the current alternate. With the advanced angle, the commutation reactance and back EMF are lower. There are three commutation angles to be controlled: the advanced-ON angle $\alpha_{\rm on}$, the advanced-reverse angle $\alpha_{\rm rvs}$, and the advanced-OFF angle $\alpha_{\rm off}$.

The advanced-ON angle is controlled in a similar manner as the turn-ON angle control of SRM [11]–[13]: $\alpha_{\rm on}$ should compensate for the angle delay of the current rising process. The expected $\alpha_{\rm on}$ that ensures $\gamma_{\rm on} = -2\pi/3$ is solved by

$$-\frac{2\pi}{3} - \alpha_{\rm on} = \frac{\psi_p (I_p, i_f, -2\pi/3) - \psi_p (0, i_f, \alpha_{\rm on})}{U/\omega} \tag{8}$$

where I_p is the chopping limit of the phase current.

By comparing Fig. 2(b) and (c), it can be seen that any advance of $\alpha_{\rm off}$ results in the loss of torque. To avoid this, $\alpha_{\rm off}$ is set to be $2\pi/3$.

The control of $\alpha_{\rm rvs}$ is the most important because the turn-reverse commutation suffers from the large inductance and direction change of the back EMF. Fig. 3 shows the three-dimensional (3-D) ideal ψ–i–θ curves of different $\alpha_{\rm rvs}$ under the front view, left view, and top view. The area $S_{i\psi}$ enclosed by the ψ–i curve equals the energy converted by the electromechanical process in one electric cycle

$$S_{i\psi} = \oint i_p d\psi_p = 2\pi T_{\rm pave}/N_r \tag{9}$$

where $T_{\rm pave}$ is the single-phase average torque. The area $S_{i\psi}$ is proportional to $T_{\rm pave}$. Commutation torque loss is marked by the shaded area on the lower right of Fig. 3.

C. Synchronized Zero Crossing

An appropriate $\alpha_{\rm rvs}$ can reduce the torque loss and torque ripple. Properly choosing $\alpha_{\rm rvs}$ is a multiobjective optimization problem. The analytical solution of the exact optimal $\alpha_{\rm rvs}$ can hardly be deduced using a nonlinear model. Nevertheless, the optimal solutions satisfy the condition $\gamma_{\rm rvs} \approx 0$, for the following reasons.

1) Fig. 2 shows that no negative T_{pf} is produced when $\gamma_{\rm rvs} = 0$, which means the torque ripple is small.
2) Fig. 3 shows that the torque loss is small when $\gamma_{\rm rvs} = 0$.

Based on the judgment that $\alpha_{\rm rvs}$ is approximately optimal when $\gamma_{\rm rvs} = 0$, the multiobjective optimization problem is transformed into a control problem with the optimal reference $\gamma_{\rm rvs} = 0$.

During the turn-reverse commutation, with $u_p = -U$ and boundary conditions substituted into (7), i_p is solved as

$$i_p = (-U\theta/\omega - i_f L_{pf}(\theta) + C_{ip}) / L_p(\theta) \tag{10}$$

$$\begin{aligned} C_{ip} &= U\alpha_{\rm rvs}/\omega + \psi_p (I_p, i_f, \alpha_{\rm rvs}) \\ &= U\gamma_{\rm rvs}/\omega + \psi_p (0, i_f, \gamma_{\rm rvs}) . \end{aligned} \tag{11}$$

Equations (10) and (11) are linearized according to (1)–(4), and the mathematical relationship between $\alpha_{\rm rvs}$ and $\gamma_{\rm rvs}$ is solved as

$$\gamma_{\rm rvs} = \frac{[k_\psi (I_p, i_f) + U/\omega]\,\alpha_{\rm rvs} + L_{\rm pmax} I_p}{(\gamma_{\rm rvs}/|\gamma_{\rm rvs}|)\, i_f k_{Lpf} + U/\omega} \tag{12}$$

where k_ψ is defined by

$$k_\psi (I_p, i_f) = \frac{(L_{\rm pmax} - L_{\rm pmin}) I_p + (L_{\rm pfmax} - L_{\rm pfmin}) i_f}{2\pi/3} . \tag{13}$$

When $\gamma_{\rm rvs} \approx 0$, (12) becomes

$$\gamma_{\rm rvs} \approx \frac{k_\psi (I_p, i_f) + U/\omega}{U/\omega}\alpha_{\rm rvs} + \frac{L_{\rm pmax} I_p}{U/\omega} . \tag{14}$$

III. Three-Phase SCC

A. Vector Control Strategy

The single-phase commutation control in the previous section can be extended to the three-phase case. Fig. 4 shows the simplified 3-slot/2-pole structure of the three-phase DSM. Considering the constraint $i_a + i_b + i_c = 0$, Fig. 5 illustrates the

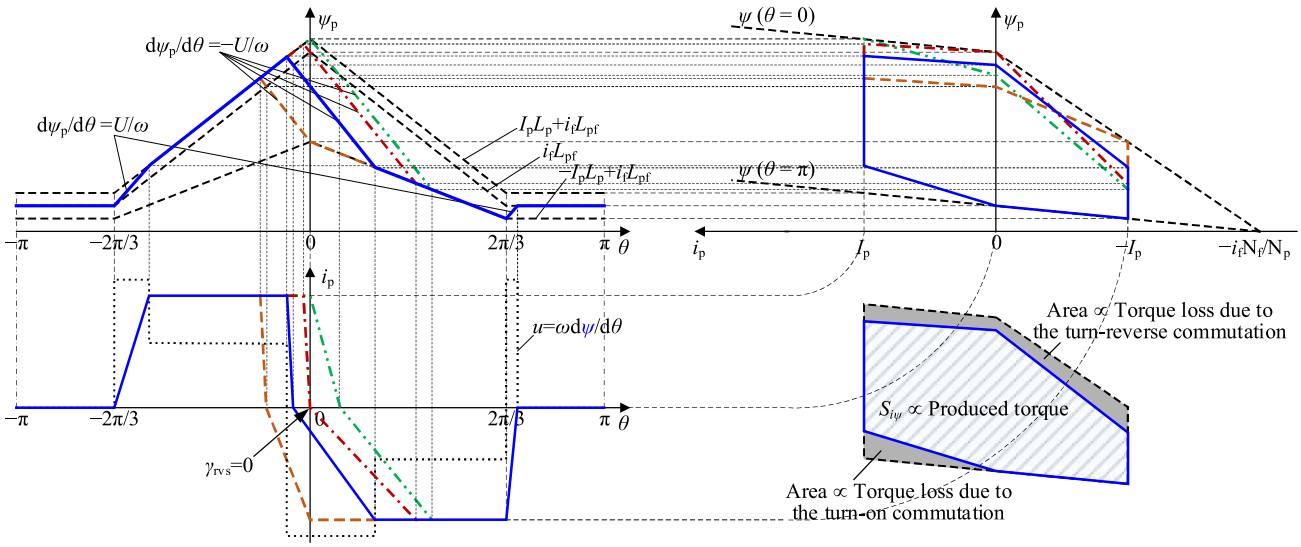

Fig. 3. Three views of the linearized 3-D ψ–i–θ curves of different advanced reverse angles.

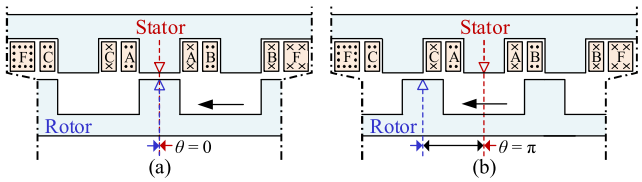

Fig. 4. Simplified 3-slot/2-pole structure of the three-phase DSM.

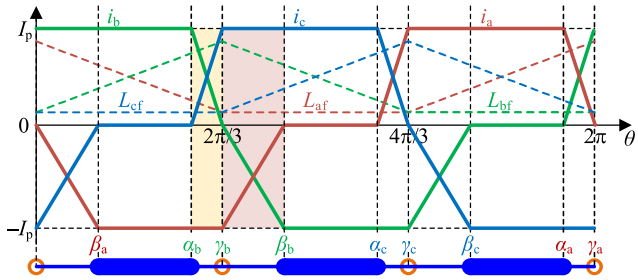

Fig. 5. Linearized current waveforms of the three-phase SCC.

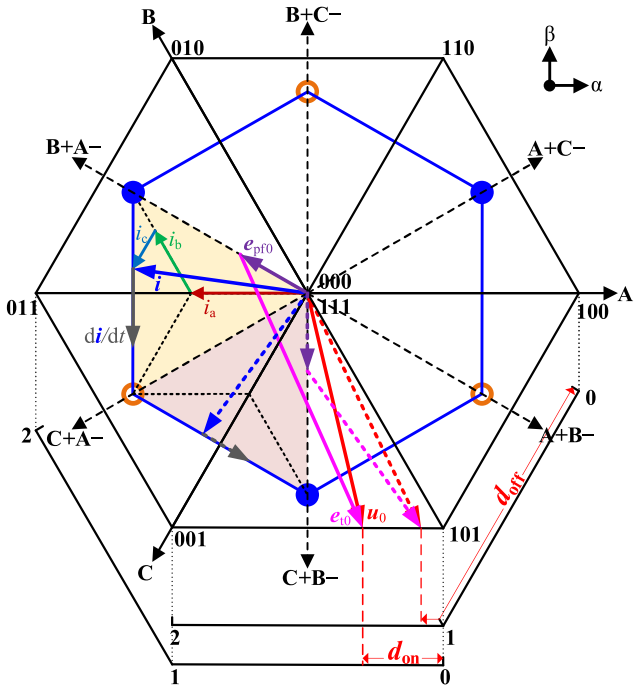

Fig. 6. Vector diagram of the control plane with the hexagonal current vector trajectory. The vectors of the turn-ON commutation are marked by solid arrows. The vectors of the turn-OFF commutation are marked by dashed arrows.

desired three-phase current with the optimized commutation. The current zero crossings are all synchronous with the peak inductances. Each of the three-phase currents reaches I_p when the inductance starts to rise, crosses 0 when the inductance is the maximum, and leaves $-I_p$ when the inductance reaches the minimum. The turn-ON commutation of i_c is in parallel with the front half of the turn-reverse commutation of i_b, and the latter half of the turn-reverse commutation of i_b is in parallel with the turn-OFF commutation of i_a.

The constraint $i_a + i_b + i_c = 0$ defines the 2-D control plane in the three-phase Cartesian coordinate system. Fig. 6 illustrates the relationship between the current vector, the phase voltage vector, and the back EMF vector on the control plane during the commutation process, where $\boldsymbol{i} = (i_a, i_b, i_c)$ is the current vector and $\boldsymbol{u}_0$, $\boldsymbol{e}_{pf0}$, and $\boldsymbol{e}_{t0}$ are the projections of, respectively, the vectors $\boldsymbol{u} = (u_a, u_b, u_c)$, $\boldsymbol{e}_{pf} = (e_{af}, e_{bf}, e_{cf})$, and $\boldsymbol{e}_t = (e_{at}, e_{bt}, e_{ct})$ on the control plane. The coordinates of the vectors $\boldsymbol{u}_0$, $\boldsymbol{e}_{pf0}$, and $\boldsymbol{e}_{t0}$ on the control plane are the Clarke transform of the coordinates of the vectors $\boldsymbol{u}$, $\boldsymbol{e}_{pf}$, and $\boldsymbol{e}_t$, respectively. The current vector trajectory that corresponds to the waveforms in Fig. 5 shapes the regular hexagon in Fig. 6, where the noncommutation-state current vectors are marked out by the solid circles, and the zero crossing current vectors are marked

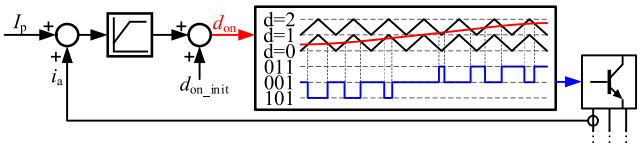

Fig. 7. Three-level PWM strategy during the turn-ON commutation when i_b falls from I_p to 0.

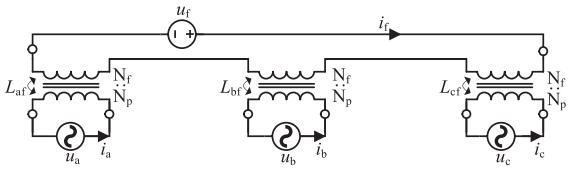

Fig. 8. Equivalent circuit of DSM considering the variation of field current.

out by the hollow circles. In one electric cycle, the current vector rotates counterclockwise along the regular hexagon. When the three-phase currents do not commutate, the current vector stays still at the solid circle. The turn-ON commutation is the edge of the regular hexagon from the solid circle to the hollow circle, and the turn-OFF commutation is the edge from the hollow circle to the solid circle. Ignoring e_{pr} in (6), the relationship between the vectors $\boldsymbol{u}$, $\boldsymbol{e}_{pf}$, and $\boldsymbol{e}_t$ is simplified as

$$\boldsymbol{u} \approx \boldsymbol{e}_{pf} + \boldsymbol{e}_t. \tag{15}$$

$\boldsymbol{e}_{pf}$ can be estimated as

$$\boldsymbol{e}_{pf} \approx (-Ud_{ss}/2, Ud_{ss}/2, 0) \tag{16}$$

where d_{ss} is the noncommutation-state duty cycle, and U is the dc-bus voltage. During the process when i_b falls from I_p to 0, the desired d$\boldsymbol{i}$/dt should be along the edge of the regular hexagon

$$d\boldsymbol{i}/dt = (0, di_b/dt, di_c/dt) = (0, di_b/dt, -di_b/dt). \tag{17}$$

Then, the transformer EMF vector is calculated as

$$\boldsymbol{e}_t = (L_a, L_b, L_c)\left(\frac{d\boldsymbol{i}}{dt}\right)^T \approx \left(0, L_{\text{pmax}}\frac{di_b}{dt}, -L_{\text{pmin}}\frac{di_b}{dt}\right). \tag{18}$$

The modulated voltage vector $\boldsymbol{u}_0$ should be on the edge of the voltage hexagon so that the $\boldsymbol{u}_0$ can provide the maximal di_b/dt. In addition, $\boldsymbol{u}_0$ should ensure $i_a = -I_p$ so that the current vector is on the edge of the regular hexagon. The three-level pulsewidth modulation (PWM) strategy for modulating the vector $\boldsymbol{u}_0$ is shown in Fig. 7, where d_{on} is the duty cycle used to modulate the vector $\boldsymbol{u}_0$ in Fig. 6 during the turn-ON commutation. d_{on} is calculated by adding the output of the proportional–integral (PI) regulator to the analytical solution of d_{on} (denoted by $d_{\text{on\_init}}$), which is calculated according to (15)–(18) and the vector diagram as

$$d_{\text{on\_init}} = \left[(\mu_{sa}+2)\, d_{ss} + 2\right] / \left(2\mu_{sa}+2\right) \tag{19}$$

where μ_{sa} is the salient ratio defined by

$$\mu_{sa} = L_{\text{pfmax}}/L_{\text{pfmin}}. \tag{20}$$

Although the modulation strategy is designed for the generalized situation that d_{on} is in the domain [0, 2], $d_{\text{on\_init}}$ is in the domain $[0, (\mu_{sa}+4)/(2\mu_{sa}+2)]$ by substituting $d_{ss} \in [0, 1]$ into (19). Therefore, d_{on} should be limited accordingly.

Besides, for the turn-OFF commutation when i_b falls from 0 to $-I_p$, the transformer EMF vector should be

$$e_t \approx (-L_{\text{pmin}}di_b/dt, L_{\text{pmax}}di_b/dt, 0) \tag{21}$$

and the rotational EMF vector is estimated as

$$e_{pf} \approx (0, -Ud_{ss}/2, Ud_{ss}/2). \tag{22}$$

The duty cycle used to generate the voltage vector $\boldsymbol{u}_0$ during the turn-OFF commutation is d_{off} in Fig. 6. The analytical solution of d_{off} (denoted by $d_{\text{off\_init}}$) is calculated as

$$d_{\text{off\_init}} = \begin{cases} 1 + \frac{\mu_{sa}+2}{2\mu_{sa}}\left(d_{ss} - \frac{2}{\mu_{sa}+2}\right), & \text{if } d_{ss} > \frac{2}{\mu_{sa}+2} \\ 1 + \frac{\mu_{sa}+2}{2\mu_{sa}+2}\left(d_{ss} - \frac{\mu_{sa}}{\mu_{sa}+2}\right), & \text{if } d_{ss} < \frac{2}{\mu_{sa}+2}. \end{cases} \tag{23}$$

Apart from the three-level PWM shown in Fig. 7, another option for the current controller was the double-band three-level hysteresis controller [15].

B. Analytical Model Between the Advanced Angle and the Zero Crossing

During the process when i_b falls from I_p to 0, the voltage equation is

$$U = u_c - u_b = d\left(L_c i_c + L_{cf} i_f - L_b i_b - L_{bf} i_f\right)/dt. \tag{24}$$

With the constraint $i_b + i_c = -i_a = I_p$ substituted, the previous equation becomes

$$-U/\omega = d\left[\left(L_b + L_c\right) i_b - L_c I_p + \left(L_{bf} - L_{cf}\right) i_f\right]/d\theta. \tag{25}$$

The mathematical relationship between the advanced angle α_b and the zero crossing γ_b is deduced by solving the differential equation (25) with the boundary conditions $i_b(\theta = \alpha_{\text{b}}) = I_p$ and $i_b(\theta = \gamma_b \approx 2\pi/3) = 0$. The solving process is similar to the single-phase case in Section II-C. The solution is

$$\gamma_b - \frac{2\pi}{3} \approx \left[\frac{k_\psi\left(I_p, i_f\right)}{U/\omega} + 1\right]\left(\alpha_b - \frac{2\pi}{3}\right) + \frac{L_{\text{pmax}} + L_{\text{pmin}}}{U/\omega} I_p. \tag{26}$$

In most cases, the field winding is excited by a voltage source, and the variation of the field current cannot be ignored. The equivalent circuit of the voltage-source-excited DSM is shown in Fig. 8. Due to the variation of the three-phase currents, the induced voltage e_{fpt} across the field winding is

$$e_{fpt} = -L_{af}di_a/dt - L_{bf}di_b/dt - L_{cf}di_c/dt. \tag{27}$$

The increment of the field current is calculated as

$$\Delta i_f \approx \int \left(e_{fpt}/L_f\right) dt = \left(-L_{af}\Delta i_a - L_{bf}\Delta i_b - L_{cf}\Delta i_c\right)/L_f. \tag{28}$$

During the commutation when i_b falls from I_p to 0, the increment of the field current is

$$\Delta i_f \approx \left(L_{bf} - L_{cf}\right) I_p/L_f \approx \left(L_{\text{pfmax}} - L_{\text{pfmin}}\right) I_p/L_f. \tag{29}$$

By substituting (29) into the solving process, the analytical solution (26) becomes

$$\gamma_b - 2\pi/3 \approx \left[k_\psi\left(I_p, i_f\right)/\left(U/\omega\right)+1\right]\left(\alpha_b - 2\pi/3\right) + \left[L_{\mathrm{pmax}} + L_{\mathrm{pmin}} - \left(L_{\mathrm{pfmax}} - L_{\mathrm{pfmin}}\right)^2/L_f\right]\omega I_p/U. \tag{30}$$

IV. Adaptive Angle Adjustment Controller Design

To adaptively adjust the advanced angle, an additional angle loop is introduced to lock the zero crossing of the phase current.

The linearized relationships between the advanced angle α and the current zero crossing γ are deduced in previous sections. In the discrete system, those relationships are generalized into a discrete linear function as

$$\gamma\left(t\right) = k\left(t\right)\alpha\left(t\right) + b\left(t\right) \tag{31}$$

where $k(t)$ and $b(t)$ are time-varying and influenced by the speed and current, and t is the sampling time. To eliminate the static error under the constant disturbance, the control law is solved with the incremental form system model. By supposing that $k(t)$ remains unchanged between two adjacent samples, the increment of $\gamma(t)$ between the two samples is

$$\dot{\gamma}\left(t\right) = \gamma\left(t+1\right) - \gamma\left(t\right) \approx k\left(t\right)\dot{\alpha}\left(t\right) + \dot{b}\left(t\right) \tag{32}$$

where

$$\dot{\alpha}\left(t\right) = \alpha\left(t+1\right) - \alpha\left(t\right) = \alpha\left(t\right)\left(q-1\right) \tag{33}$$

$$\dot{b}\left(t\right) = b\left(t+1\right) - b\left(t\right) = b\left(t\right)\left(q-1\right) \tag{34}$$

where q is the delay operator. By solving

$$\gamma\left(t+1\right) = \gamma\left(t\right) + \dot{\gamma}\left(t\right) = 0 \tag{35}$$

the control law is obtained as

$$\dot{\alpha}\left(t\right) = \left[-\gamma\left(t\right) - \dot{b}\left(t\right)\right]/k\left(t\right). \tag{36}$$

In the three-phase voltage-source-excited case, according to (30), the estimated *k* and *b* are

$$\hat{k} = \left[k_\psi\left(I_p, i_f\right)\right]/\left(U/\omega\right)+1 \tag{37}$$

$$\hat{b} = \left[L_{\mathrm{pmax}} + L_{\mathrm{pmin}} - \left(L_{\mathrm{pfmax}} - L_{\mathrm{pfmin}}\right)^2/L_f\right]\omega I_p/U. \tag{38}$$

After integrating both sides of (36) by multiplying $q^{-1}/(1-q^{-1})$ and substituting estimated parameters, the control law becomes

$$\alpha\left(t\right) = \underbrace{-\frac{\gamma\left(t\right)}{\hat{k}\left(t\right)}\frac{q^{-1}}{1-q^{-1}}}_{\text{adaptive}} \underbrace{-\frac{\hat{b}\left(t\right)}{\hat{k}\left(t\right)}}_{\text{analytical}} \tag{39}$$

where the adaptive term adjusts α according to the feedback, and the analytical term is the analytical solution of α by substituting $\gamma = 0$ into (31).

Due to the inaccuracy of the simplified model, the system risks instability. The system is also affected by random high-frequency disturbances because of the differences in adjacent commutations.

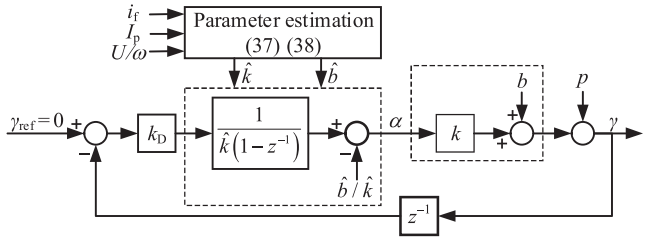

Fig. 9. Diagram of the synchronous zero-crossing control system.

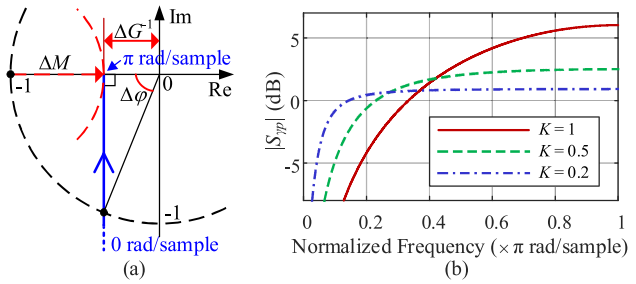

Fig. 10. Frequency domain characteristic of the system. (a) Nyquist diagram. (b) Frequency responses of $S_{\gamma p}$ with different loop gains.

To improve system robustness and suppress disturbances, a damp parameter k_D $(0 < k_D < 1)$ is connected to the forward path to reduce the loop gain. The control law with k_D is

$$\alpha\left(t\right) = \underbrace{-\frac{k_D\gamma\left(t\right)}{\hat{k}\left(t\right)}\frac{q^{-1}}{1-q^{-1}}}_{\text{adaptive}} \underbrace{-\frac{\hat{b}\left(t\right)}{\hat{k}\left(t\right)}}_{\text{analytical}} \tag{40}$$

namely

$$\alpha\left(t\right) = \underbrace{\alpha\left(t-1\right) - \frac{k_D\gamma\left(t-1\right)}{\hat{k}\left(t\right)}}_{\text{adaptive}} \underbrace{-\left[\frac{\hat{b}\left(t\right)}{\hat{k}\left(t\right)} - \frac{\hat{b}\left(t-1\right)}{\hat{k}\left(t-1\right)}\right]}_{\text{analytical}}. \tag{41}$$

The transfer function in the z domain is obtained by replacing q^{-1} in (39) with z^{-1}. The system diagram is shown in Fig. 9, where the lumped disturbance is denoted by p. The open-loop transfer function of the system is

$$H_{\mathrm{OL}}\left(z^{-1}\right) = kk_Dz^{-1}\Big/\left[\hat{k}\left(1-z^{-1}\right)\right]. \tag{42}$$

The Nyquist diagram of H_{OL} is shown in Fig. 10(a). The stability condition is that the loop gain K is between 0 and 2

$$0 < K = kk_D/\hat{k} < 2. \tag{43}$$

The stability margins of the system are

$$\text{gain margin } \Delta G = 2/K \tag{44}$$

$$\text{phase margin } \Delta\varphi = \arctan\sqrt{\left(4-K^2\right)/K^2} \tag{45}$$

and

$$\text{modulus margin } \Delta M = -\left|S_{\gamma p}\right|_{\max} = \left(2-K\right)/2. \tag{46}$$

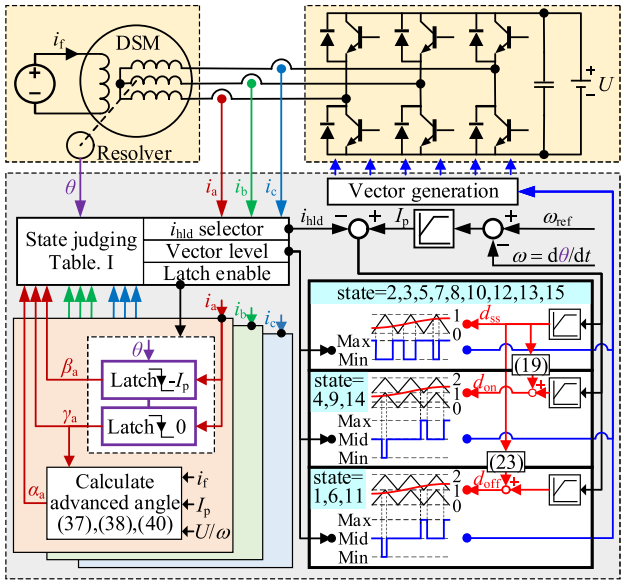

Fig. 11. System diagram of the SCC.

TABLE I
STATES AND CONTROL LOGICS

θ	State	Latch enable (1-enabled) γ latch A	B	C	β latch A	B	C	i_{hld}	Modulation logic Vector level Min	Mid	Max
0~β_a	1	1	0	0	1	0	0	i_b	001	011	010
β_a~π/3	2	0	0	0	0	0	0	i_b	11-	/	01-
π/3~α_b	3	0	0	0	0	0	0	$-i_a$	00-	/	01-
α_b~γ_b	4	0	1	0	0	0	0	$-i_a$	101	001	011
γ_b~2π/3	5	0	0	0	0	0	0	$-i_a$	0-0	/	0-1
2π/3~β_b	6	0	1	0	0	1	0	i_c	100	101	001
β_b~π	7	0	0	0	0	0	0	i_c	-11	/	-01
π~α_c	8	0	0	0	0	0	0	$-i_b$	-00	/	-01
α_c~γ_c	9	0	0	1	0	0	0	$-i_b$	110	100	101
γ_c~4π/3	10	0	0	0	0	0	0	$-i_b$	00-	/	10-
4π/3~β_c	11	0	0	1	0	0	1	i_a	010	110	100
β_c~5π/3	12	0	0	0	0	0	0	i_a	1-1	/	1-0
5π/3~α_a	13	0	0	0	0	0	0	$-i_c$	0-0	/	1-0
α_a~γ_a	14	1	0	0	0	0	0	$-i_c$	011	010	110
γ_a~2π	15	0	0	0	0	0	0	$-i_c$	–00	/	-10

If γ_b, γ_c and γ_a are larger than 2π/3, 4π/3, and 2π, states 5, 10, and 15, respectively, will disappear. The dash in vector 11- means that the C-phase switches are both OFF.

TABLE II
MODEL PARAMETERS USED WITH THE TESTED DSM

Maximum inductance L_{pfmax}	Minimum inductance L_{pfmin}	Turn ratio N_p/N_f
0.0035 H	0.000833 H	3/100

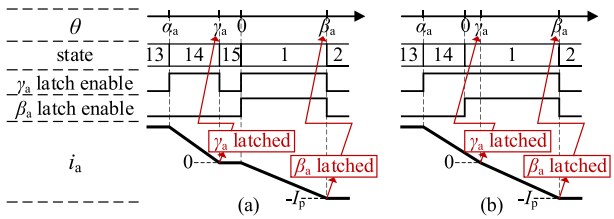

Fig. 12. State transition and angle capture sequence. (a) Case when γ_a is captured before 0. (b) Case when γ_a is captured after 0.

The smaller the loop gain K, the better the stability margins. Therefore, we can design a small k_D to reduce the loop gain to improve the stability. The transfer function from the disturbance to the output is

$$S_{\gamma p}\left(z^{-1}\right) = \left(1 - z^{-1}\right) / \left[1 - (1 - K)\, z^{-1}\right]. \quad (47)$$

The frequency responses of $S_{\gamma p}$ with different loop gains are compared in Fig. 10(b). The additional damp parameter also decreases the high-frequency gain of $S_{\gamma p}$. This can suppress the random steady-state high-frequency disturbance. However, the dynamic performance decreases because the response speed for rejecting the high-frequency disturbance decreases. k_D can be designed relatively small to achieve high levels of robustness without much impact on the dynamic performance because the disturbance caused by the change of motor speed or torque can be responded to with the analytical term of (40).

V. IMPLEMENTATION

The three-phase SCC was implemented, and the system diagram is shown in Fig. 11. The state judging and control logics are provided in Table I. The maximum inductance L_{pfmax}, the minimum inductance L_{pfmin}, and the turn ratio N_p/N_f were required for setting up the control system, and the parameters used with the tested DSM are shown in Table II, where the inductances were calculated with a finite-element simulation.

Fig. 12 shows the state transition and the angle capture process during the turn-reverse commutation of i_a. The angles γ and β were captured by latching the rotor position signal θ when the current reached 0 and $-I_p$, respectively. In the common case, the angle capture has delays. The delay in γ capture is in the feedback pathway of the angle loop, which will cause an additional error that cannot be corrected by the adaptive controller. The delays in γ and β capture will cause a state transition delay between the commutation state and the noncommutation state, which results in overshooting of the current. These delays should be minimized as much as possible in the implementation.

When the state transfers, the voltage vector changes, and there is a step disturbance in the current loop. Most of the disturbance can be compensated for by calculating $d_{\text{on\_init}}$ and $d_{\text{off\_init}}$ based on the linear model. The rest disturbance is corrected by the PI controller. However, when the commutation time is small, there is not enough time for the PI controller to reach the steady state, and additional nonlinear compensation is required in order for the current to be well chopped at I_p during the commutation. In the verifications presented in the next section, we have added the additional nonlinear compensation for the current to be well shaped. In practice, nonlinear compensation is difficult to implement, and the performance of the SCC will decrease when the commutation time is small.

In Table I, if $\alpha_a = \gamma_a = \beta_a = 0$, the method will reduce into the conventional standard control (STD). In the commutation control of STD, the phase current has a step reference, which may cause the overshoot and oscillation of the current. One

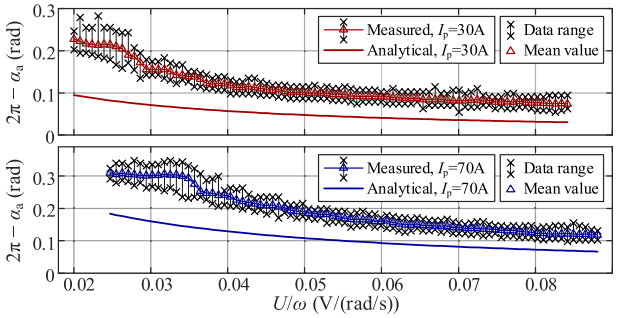

Fig. 13. Experimentally measured $2\pi-\alpha_a$ and the analytically calculated $2\pi-\alpha_a$, which both ensure synchronized zero crossing.

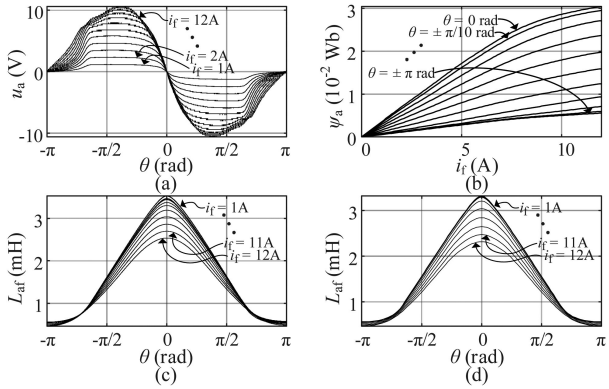

Fig. 14. Motor model identification. (a) Measured A-phase EMF on the u–θ plane when $\omega = 837.8$ rad/s, $i_f = 1, 2, \ldots, 12$ A. (b) Identified ψ_a–i_f when $\theta = 0, \pm\pi/10, \ldots, \pm\pi$ rad. (c) Identified L_{af} when $i_f = 1, 2, \ldots, 12$ A. (d) Simulated L_{af} when $i_f = 1, 2, \ldots, 12$ A.

advantage of the proposed SCC is that it does not have the step reference. However, there may be the overshoot and oscillation of the current due to the state transition delay. Although there is no step reference, it is the PI controller's responsibility to correct the possible overshoot and any other disturbances. When designing the PI parameters, the method in [16] was consulted.

A three-level hysteresis current controller was not implemented, but it is conceivable that the current could be well shaped by a hysteresis controller because there is no need for nonlinear compensation and PI parameter design.

When establishing the model, voltage drops on the power switches and other parasitic resistances, and leakage inductance of the end winding and other parasitic inductances, were not considered. Therefore, the analytically calculated angle was smaller than required. This error is related to the application conditions. Under the conditions of our test rig, the experimentally measured $2\pi-\alpha_a$ and the analytically calculated $2\pi-\alpha_a$, which both ensured $\gamma_a = 0$ under the different voltage speed ratios were shown in Fig. 13. The measured $2\pi-\alpha_a$ was approximately twice the analytical $2\pi-\alpha_a$. For better dynamic performance, (38) was calibrated by multiplying by 2. In practice, if necessary, this calibration should be conducted according to the actual conditions.

VI. Verification

The no-load constant-speed generation experiment was first conducted on the tested three-phase 12-slot/8-pole DSM. The phase flux linkage and mutual inductance were identified as

$$\psi_p(0, i_f, \theta) = \int_{-\pi}^{\theta} \frac{u_p(\omega, i_f, t)}{\omega} d\theta + \psi_p(0, i_f, -\pi) \quad (48)$$

$$L_{pf}(0, i_f, \theta) = \psi_p(0, i_f, \theta)/i_f \quad (49)$$

where $u_p(\omega, i_f, t)$, i_f, and ω were measured from experiments and $\psi_p(0, i_f, -\pi)$ was obtained by finite-element simulation. The measured A-phase EMF curves under the different field currents are shown in Fig. 14(a). The identified A-phase flux linkage curves of different rotor positions are shown in Fig. 14(b), where the magnetic saturation was at about $i_f = 7$ A. The identified L_{af} profiles are shown in Fig. 14(c), and the inductance profiles simulated by the finite element method are shown in Fig. 14(d).

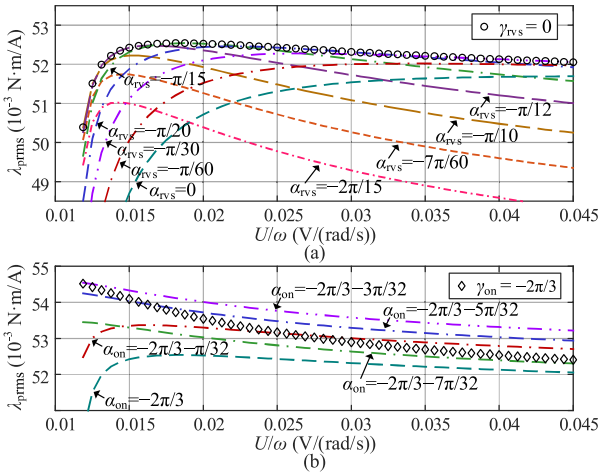

Fig. 15. Simulated torque to rms current ratio of different U/ω at $I_p = 70$ A, $i_f = 7$ A, and $\alpha_{off} = 2\pi/3$. (a) Fixed $\alpha_{on} = -2\pi/3$, different α_{rvs}. (b) Synchronized $\gamma_{rvs} = 0$, different α_{on}.

The three phases were slightly different from each other, and the other two phases were identified in the same way.

For the single-phase case, based on the identified A-phase flux linkage and the mathematical model in Section II, a simulation was conducted to verify the advantage of the synchronous control. For each combination of the input parameters α_{on}, α_{rvs}, and U/ω, the process of an electric cycle was simulated. The output was the single-phase torque to root-mean-square (rms) current ratio, which was calculated as

$$\lambda_{prms} = T_{pave}/I_{prms} = N_r \left(\oint i_p d\psi_p \right) / 2\pi / I_{prms} \quad (50)$$

where $N_r = 8$, I_{prms} was the single-phase rms current, and ψ_p was calculated as

$$\psi_p(i_p, i_f, \theta) \approx \psi_p(0, i_f + N_p i_p / N_f, \theta). \quad (51)$$

The simulation results of the fixed $\alpha_{on} = -2\pi/3$ and different α_{rvs} are shown in Fig. 15(a), where λ_{prms} of the synchronous control ($\gamma_{rvs} = 0$) approximates the envelope of the λ_{prms}

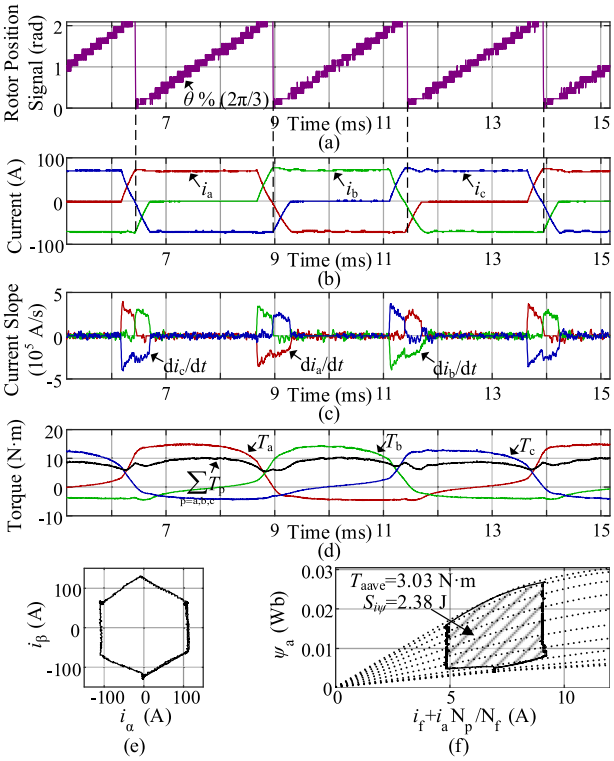

Fig. 16. Experimental waveforms of SCC under low voltage speed ratio [$I_p = 70$ A, $i_f = 7$ A, $U/\omega = 30.0$ V/(837.8 rad/s)]. (a) Measured rotor position signal. (b) Measured three-phase currents. (c) Three-phase current slopes. (d) Three-phase instantaneous torques. (e) Current vector trajectory. (f) A-phase flux linkage-current trajectory.

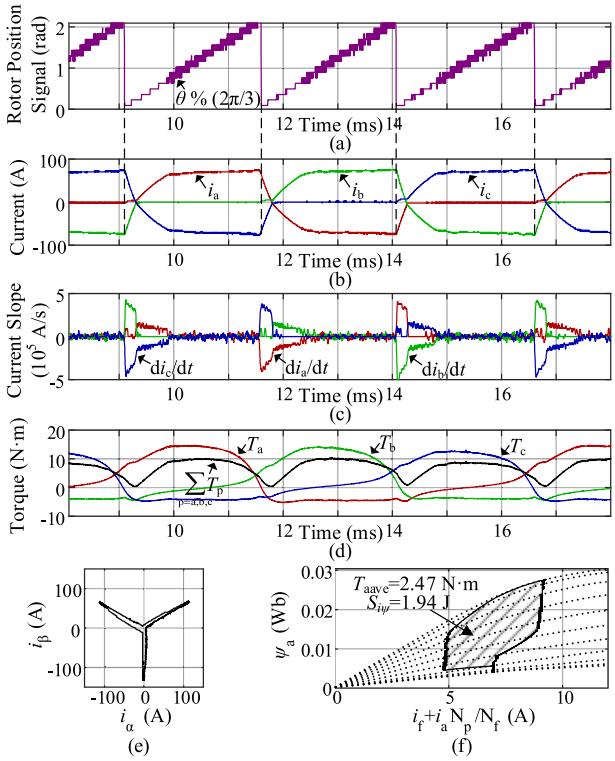

Fig. 17. Experimental waveforms of STD under low voltage speed ratio [$I_p = 70$ A, $i_f = 7$ A, $U/\omega = 30.0$ V/(837.8 rad/s)]. (a) Measured rotor position signal. (b) Measured three-phase currents. (c) Three-phase current slopes. (d) Three-phase instantaneous torques. (e) Current vector trajectory. (f) A-phase flux linkage-current trajectory.

curves of the different $\alpha_{\rm rvs}$. This verifies the effectiveness of the optimization. The simulation results of the synchronized $\gamma_{\rm rvs} = 0$ and different $\alpha_{\rm on}$ are shown in Fig. 15(b), where the optimal $\alpha_{\rm on}$ is at about $-2\pi/3{-}3\pi/32$, and $\lambda_{\rm prms}$ of the synchronous control ($\gamma_{\rm on} = -2\pi/3$) is not the optimum. This is because of the nonlinear characteristic shown in Fig. 14(a), where the EMFs are not zero before $-2\pi/3$. Hence, there is no need for the synchronous control of $\gamma_{\rm on}$. However, in the three-phase commutation control, the turn-ON commutation of the A-phase current and the turn-reverse commutation of the C-phase current affect each other. In order to achieve high overall performance of optimization and maintain the simplicity of the control strategy, it is necessary to make a concession. Therefore, the three-phase SCC method presented in Section III can still provide good overall performance.

The three-phase SCC was implemented and verified by the experiment, and the experimental waveforms of SCC and STD are compared in Figs. 16 and 17. In SCC, the commutation was well synchronized: the angles $\gamma_{\rm on}$ and $\gamma_{\rm rvs}$ of the three phases were all synchronous with the rotor position signal; the turn-ON commutation was in parallel with the front half of the turn-reverse commutation; the turn-OFF commutation was in parallel with the latter half of the turn-reverse commutation; the rising and falling rate of the two currents in commutation were the same; and the third phase was without any undercurrent or overcurrent. The current vector trajectory of SCC was well shaped to follow the regular hexagon. In STD, the angles $\gamma_{\rm on}$ and $\gamma_{\rm rvs}$ lagged the rotor position signal. The turn-OFF commutation completed first, whereas the turn-ON commutation lagged behind. Comparing the di/dt curves of the two methods, we can see that the di/dt of the turn-ON commutation and latter-half turn-reverse commutation were increased by SCC. As shown in Fig. 17(e), during the commutation, the current vector of STD was decreased to a point that was very close to the origin. Very little instantaneous torque could be produced at this point, so the commutation torque loss of this point was large. The A-phase flux linkage-current trajectories were calculated by (51) and are compared in Figs. 16(f) and 17(f). The area enclosed by the flux linkage-current trajectory of SCC was larger than that of STD, showing that the average output torque of SCC was larger. According to Fig. 3, the improvement came from the reduced torque loss during the turn-ON commutation and the turn-reverse commutation. The instantaneous torques are compared in Figs. 16(d) and 17(d). They were calculated from experimental data by the partial differentiation of magnetic co-energy W_p as

$$T_p = \frac{\partial W_p}{\partial \theta} \approx \frac{\partial \left[\int_0^{i'_p(\theta)} \psi_p\left(i'_p, 0, \theta\right) di'_p\right]}{\partial \theta}, i'_p = i_p + \frac{N_f i_f}{N_p} \tag{52}$$

where ψ_p was identified from the generation experiment, and i_p and i_f were measured in the motoring experiment. Due to the reduced torque loss during the commutation, the overall torque ripple of SCC was lower.

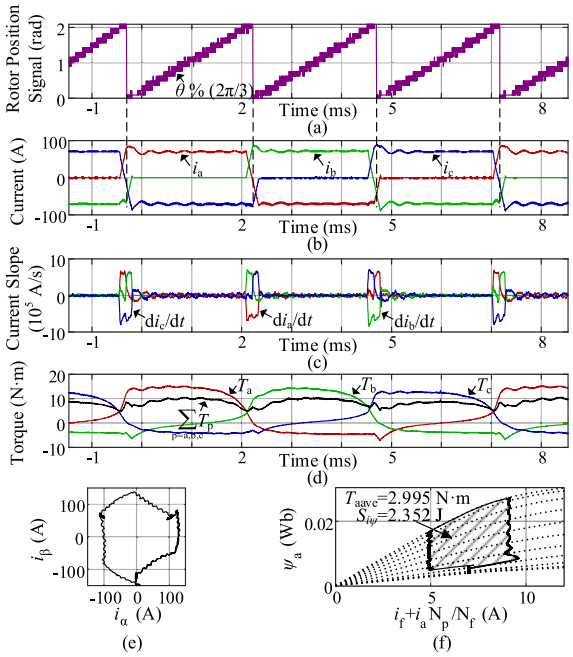

Fig. 18. Experimental waveforms of SCC under high voltage speed ratio [$I_p = 70$ A, $i_f = 7$ A, $U/\omega = 70.2$ V/(837.8 rad/s)]. (a) Measured rotor position signal. (b) Measured three-phase currents. (c) Three-phase current slopes. (d) Three-phase instantaneous torques. (e) Current vector trajectory. (f) Flux linkage-current trajectory.

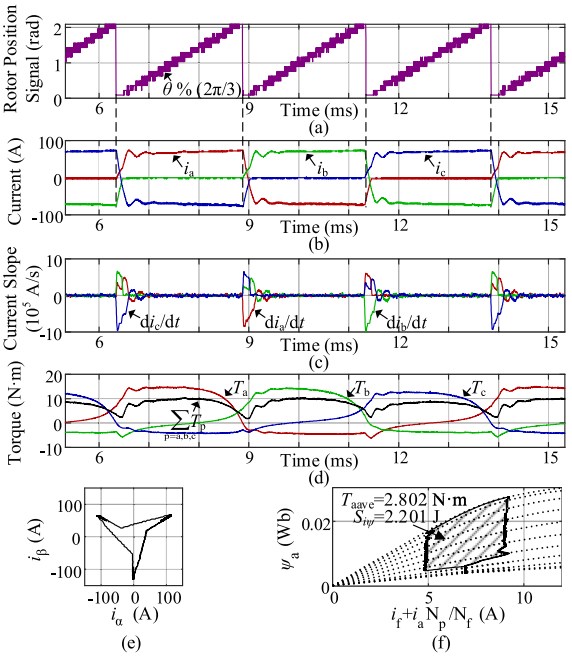

Fig. 19. Experimental waveforms of STD under high voltage speed ratio [$I_p = 70$ A, $i_f = 7$ A, $U/\omega = 70.1$ V/(837.8 rad/s)]. (a) Measured rotor position signal. (b) Measured three-phase currents. (c) Three-phase current slopes. (d) Three-phase instantaneous torques. (e) Current vector trajectory. (f) Flux linkage-current trajectory.

The experimental results of SCC and STD at the higher voltage speed ratio are compared in Figs. 18 and 19. The advantage of the proposed SCC was not that significant because the commutation time was small. Both methods had the overshoot and oscillation of the current after the commutation. As explained in Section V, the overshoot and oscillation in SCC were because of the state transition delays, and the overshoot and oscillation in STD came from the step reference.

Fig. 20 compares more experimental results of the torque to rms current ratio and torque ripple performance. The torque ripple performance was evaluated by

$$\mu_T = \frac{\max T_\Sigma - \min T_\Sigma}{\text{mean} T_\Sigma} \times 100\%,\ T_\Sigma = \sum_{p=a,b,c} T_p. \quad (53)$$

λ_{arms} of SCC were all larger than that of STD, and μ_T of SCC were all lower than STD, which shows that SCC could improve torque-to-current ratio and torque ripple performance at a wide range of speeds. The improvement came from the reduced commutation torque loss. When the voltage speed ratio was low or the current amplitude was large, the commutation time was long and the commutation torque loss was large, so the improvement was large.

The performance of the closed-loop controller was verified by the step response of speed. The driven load was a doubly salient generator whose field current and load resistance remained unchanged in the experiment, so the output power of the generator increased quadratically with speed; hence, the load torque of the motor would increase with speed. When there was a step-speed reference, the current amplitude I_p suddenly increased to the saturated value and the speed ω increased with the maximum acceleration. Between the variables I_p, i_f, and ω, I_p was the source of the most severe disturbance because the armature winding had the minimum time constant.

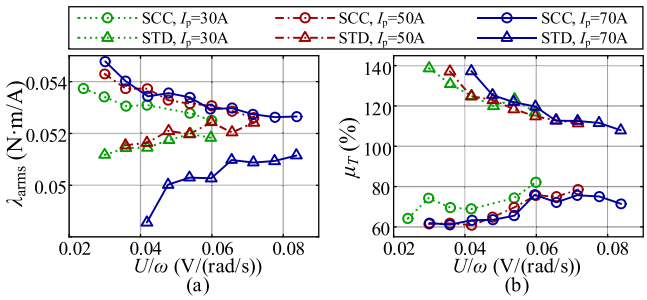

Fig. 20. Comparison of the different control methods at $i_f = 7$ A. (a) A-phase torque to rms current ratio. (b) Torque ripple.

Fig. 21 compares the speed step responses of the different damp parameters k_D. All the results show that α_a could respond to the disturbance of the step-speed reference, and γ_a could be locked at about 0. This shows that the optimized points of SCC in Fig. 20 can be adaptively reached when the speed and current change. But on the α_a and γ_a curves, there was some random disturbance at the steady state, especially at high speed. The disturbance on γ_a was large, whereas the disturbance on α_a was small. This shows that the system was disturbed between α_a and γ_a. Comparing the results with different k_D in Fig. 21, we can see that the disturbances decreased with the decrease of k_D. This is because the small k_D can weaken the influence of γ_a on

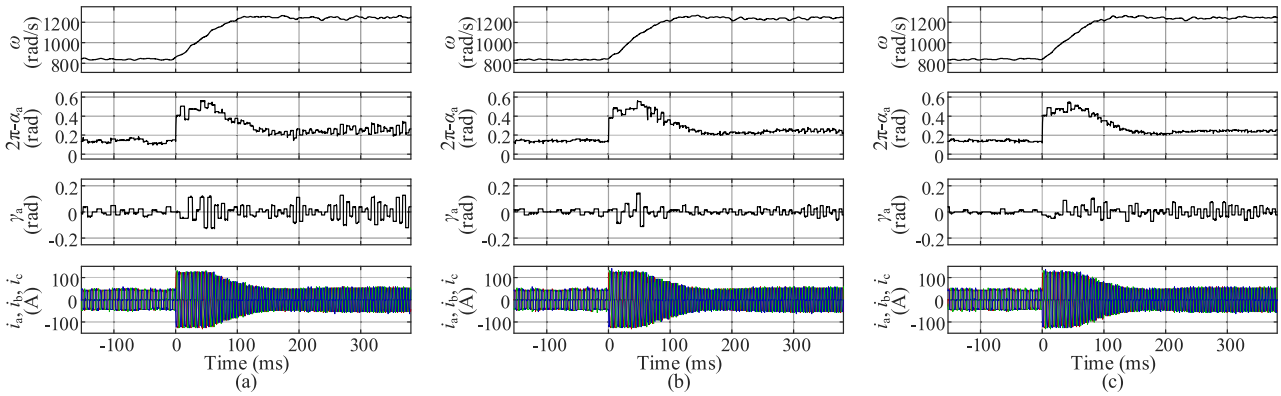

Fig. 21. Experimental speed step response of the system with the different damp parameters, the reference ω steps from 837.8 to 1256.6 rad/s at time = 0 ($i_f = 4.78$ A, $U = 41.6$ V when $\omega = 837.8$ rad/s, $U = 39.4$ V when $\omega = 1256.6$ rad/s). (a) $k_D = 1$. (b) $k_D = 0.5$. (c) $k_D = 0.2$.

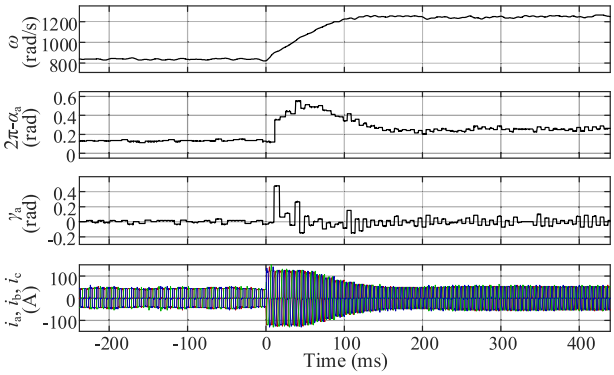

Fig. 22. Experimental speed step response of the model-free system, the reference ω steps from 837.8 to 1256.6 rad/s at time = 0 ($k_D = 0.5$, $i_f = 4.78$ A, $U = 42.0$ V when $\omega = 837.8$ rad/s; $U = 39.9$ V when $\omega = 1256.6$ rad/s).

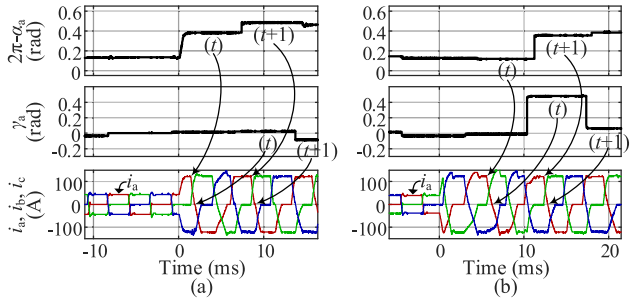

Fig. 23. Comparison of the details of the speed step response of the differently designed systems, where (t) denotes the first electric cycle after the reference ω changes, and $(t + 1)$ denotes the cycle after (t). (a) Details of Fig. 21(b), model-based design. (b) Details of Fig. 22, model-free design.

α_a, and further prevent the disturbances from being amplified by the closed loop. When $k_D = 0.5$, the disturbance on the advanced angle was small enough, and there was no significant improvement when $k_D = 0.2$. The difference is small between the dynamic performances of different k_D. This is because the dynamic disturbance from the step-speed reference was mainly dealt with by the analytical term of the control law. As a result, the damp parameter k_D was designed to be 0.5 in this case. According to (44)–(46), assuming that the estimation of k was accurate, $k_D = 0.5$ offered a gain margin of 4 (12 dB), a phase margin of 75.5°, and a modulus margin of 0.75 (−2.5 dB).

In addition, the system can be model-free and without any estimation of the model parameters k and b, by using the control law

$$\alpha(t) = \alpha(t-1) - k_D \gamma(t-1). \tag{54}$$

Fig. 22 shows the step response of the model-free system with $k_D = 0.5$. The model-free system could also work well. However, without the adaptive term, the dynamic performance will be poor. Fig. 23 compares the details of the normally designed system and the model-free system. The response of the model-free system was one cycle slower, and there were larger errors during the dynamic process. Moreover, the model-free system risks higher instability. Therefore, k_D should be designed lower so that the system can have a larger margin of stability, although the lower k_D makes the dynamic performance even worse.

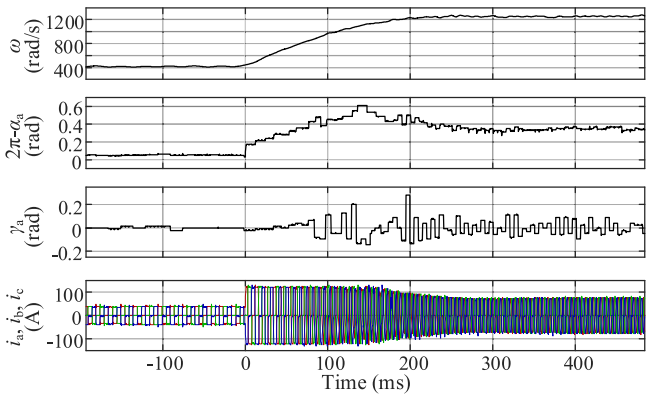

Fig. 24. Experimental speed step response, the reference ω steps from 418.9 to 1256.6 rad/s at time = 0 ($k_D = 0.5$, $i_f = 6.95$ A, $U = 43.1$ V when $\omega = 418.9$ rad/s; $U = 35.2$ V when $\omega = 1256.6$ rad/s).

Fig. 24 shows the response of a larger reference speed step under the bigger load torque. The system also had high dynamic performance, although the steady-state disturbance on γ_a was greater than with the lower speed and smaller load, which can be seen by comparing Figs. 21(b) and 24. This shows that random disturbances are large when the speed and current are high.

The random disturbances came from the uncertainties of the commutation process, which were not modeled by (30). When speed or current increases, the commutation time is longer, and there will be more uncertainties and disturbances. In order to ensure stability and suppress disturbances, the parameter k_D should be designed, in practice, according to the worst case.

VII. Conclusion

In this article, the SCC method is proposed to improve the commutation control of a doubly salient motor. The commutation angle is adaptively optimized by the angle loop that locks the zero-crossing point of the phase current. No matter what the working conditions are (typically speed, field current, and load torque), appropriate advanced angles can always be generated to reduce the commutation torque loss. Compared with the model-based AOM, the accurate model is not required. A controller with desirable robustness can be developed using only a small amount of model information that does not necessarily have to be very accurate: the maximum and minimum inductance and the turn ratio between the field coil and the armature coil. Furthermore, the vector control strategy is adopted in the proposed method to shape the three-phase currents during the commutation. In general, this method provides a solution for the high-performance commutation control of DSM, and can be applied in DSM drive systems that demand a high torque-to-current ratio and low-torque ripple in a wide range of speeds, such as with electric vehicles.

References

[1] Y. F. Liao, F. Liang, and T. A. Lipo, "A novel permanent magnet motor with doubly salient structure," *IEEE Trans. Ind. Appl.*, vol. 31, no. 5, pp. 1069–1078, Sep./Oct. 1995.

[2] L. Yu, Z. R. Zhang, Z. H. Cheng, and Y. G. Yan, "Analysis and verification of the doubly salient brushless DC generator for automobile auxiliary power unit application," *IEEE Trans. Ind. Electron.*, vol. 61, no. 12, pp. 6655–6663, Dec. 2014.

[3] F. Blaabjerg, L. Christensen, P. O. Rasmussen, L. Oestergaard, and P. Pedersen, "New advanced control methods for doubly salient permanent magnet motor," in *Proc. IEEE Ind. Appl . Conf.*, 1995, pp. 222–230.

[4] C. C. Chan, J. Z. Jiang, W. Xia, and K. T. Chau, "Novel wide range speed control of permanent magnet brushless motor drives," *IEEE Trans. Power Electron.*, vol. 10, no. 5, pp. 539–546, Sep. 1995.

[5] Y. Wang, Z. R. Zhang, R. Liang, and Y. G. Yan, "Torque density improvement of doubly salient electromagnetic machine with asymmetric current control," *IEEE Trans. Ind. Electron.*, vol. 63, no. 12, pp. 7434–7443, Dec. 2016.

[6] M. Cheng, Q. Sun, and E. Zhou, "New self-tuning fuzzy PI control of a novel doubly salient permanent magnet motor drive," *IEEE Trans. Ind. Electron.*, vol. 53, no. 3, pp. 814–821, Jun. 2006.

[7] W. Jia and L. Xiao, "Research on control strategies for doubly salient electromagnetic machine," *IET Elect. Power Appl.*, vol. 11, no. 8, pp. 1449–1456, Sep. 2017.

[8] X. X. Kong, M. Cheng, and Y. G. Shu, "Extreme learning machine based phase angle control for stator-doubly-fed doubly salient motor for electric vehicles," in *Proc. IEEE Veh. Power Propulsion Conf.*, 2008, pp. 1–5.

[9] Y. T. Chen, C. L. Chiu, Z. H. Tang, Y. L. Liang, and R. H. Liang, "Optimizing efficiency driver comprising phase-locked loop for the single-phase brushless DC fan motor," *IEEE Trans. Magn.*, vol. 48, no. 5, pp. 1937–1942, May 2012.

[10] C. Gu, X. L. Wang, X. Q. Shi, and Z. Q. Deng, "A PLL-based novel commutation correction strategy for a high-speed brushless DC motor sensorless drive system," *IEEE Trans. Ind. Electron.*, vol. 65, no. 5, pp. 3752–3762, May 2018.

[11] S. R. MacMinn and J. W. Sember, "Control of a switched-reluctance aircraft engine starter-generator over a very wide speed range," in *Proc. IEEE Intersociety Energy Convers. Eng. Conf* ., 1989, pp. 631–638.

[12] C. Mademlis and I. Kioskeridis, "Performance optimization in switched reluctance motor drives with online commutation angle control," *IEEE Trans. Energy Convers.*, vol. 18, no. 3, pp. 448–457, Sep. 2003.

[13] Y. Sozer, D. A. Torrey, and E. Mese, "Automatic control of excitation parameters for switched-reluctance motor drives," *IEEE Trans. Power Electron.*, vol. 18, no. 2, pp. 594–603, Mar. 2003.

[14] W. D. Jiang, Y. M. Liao, J. P. Wang, P. X. Wang, and Y. F. Xie, "Improved control of BLDCM considering commutation torque ripple and commutation time in full speed range," *IEEE Trans. Power Electron.*, vol. 33, no. 5, pp. 4249–4260, May 2018.

[15] P. C. Loh, G. H. Bode, D. G. Holmes, and T. A. Lipo, "A time-based double band hysteresis current regulation strategy for single phase multilevel inverters," *IEEE Trans. Ind. Appl.*, vol. 39, no. 3, pp. 883–892, May/Jun. 2003.

[16] S. S. Ahmad and G. Narayanan, "Linearized modeling of switched reluctance motor for closed-loop current control," *IEEE Trans. Ind. Appl.*, vol. 52, no. 4, pp. 3146–3158, Jul. 2016.

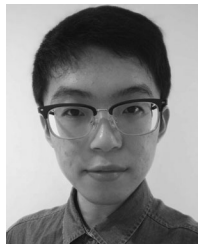

Zhangming Bian received the B.S. degree in electrical engineering in 2017 from the Nanjing University of Aeronautics and Astronautics, Nanjing, China, where he is currently working toward the M.S. degree in electrical engineering.

His main research interests include control of the doubly salient motor.

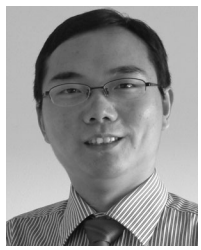

Zhuoran Zhang (M'09–SM'12) received the B.S. degree in measurement engineering and the M.S. and Ph.D. degrees in electrical engineering from the Nanjing University of Aeronautics and Astronautics (NUAA), Nanjing, China, in 2000, 2003, and 2009, respectively.

Since 2003, he has been a Faculty Member with the Department of Electrical Engineering, NUAA, where he is currently a Full Professor and the Vice-Director of Jiangsu Provincial Key Laboratory of New Energy Generation and Power Conversion. From February 2012 to June 2013, he was a Visiting Professor with Wisconsin Electric Machines and Power Electronics Consortium, University of Wisconsin-Madison, USA. From 2016 to 2017, he was with Commercial Aircraft Corporation of China, Ltd., and was appointed as the Deputy Director of electrical system designers of C919 civil jet aircraft. He has authored or coauthored more than 140 technical papers and two books, and is the holder of 35 issued patents in the research areas, which include design and control of permanent magnet machines, hybrid excitation electric machines, and doubly salient electric machines for aircraft power, electric vehicles, and renewable energy generation.

Li Yu (S'15–M'19) received the B.S. degree in electrical engineering from the Nanjing University of Technology, Nanjing, China, in 2011, and the M.S. and Ph.D. degrees in electrical engineering from the Nanjing University of Aeronautics and Astronautics (NUAA), Nanjing, China, in 2014 and 2019, respectively.

From March 2018 to March 2019, he was a Visiting Ph.D. Student with the Power Electronics, Machine, and Control Group, The University of Nottingham, Nottingham, U.K. Since 2019, he has been a Lecturer with the Department of Electrical Engineering, NUAA. His main research interests include the doubly salient electric machine design and control for aircraft power system.

Dr. Yu is the recipient of the Best Paper Award in IEEE 2013 Vehicle Power and Propulsion Conference.